

Polyoxovanadates as Precursors for the Synthesis of Colloidal Multi-Metal Oxide Nanocrystals

Adam J. Biacchi, Lucas M. Johnson, Ashley B. Sweet, Luke J. Barrante, Eric M. Cal, Angela R. Hight Walker, and Matthew R. Buck*



Cite This: *Chem. Mater.* 2022, 34, 2907–2918



Read Online

ACCESS |



Metrics & More

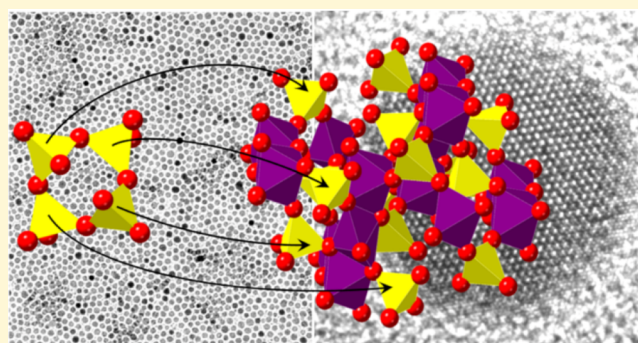


Article Recommendations



Supporting Information

ABSTRACT: Colloidal multi-metal oxide nanocrystals that contain the element vanadium are attractive materials for enabling diverse technologies. Few nanocrystal systems are synthetically well developed, however, which is attributable to a scarcity of molecular precursors that enable facile incorporation of vanadium. Here, we demonstrate the viability of polyoxovanadates as precursors for colloidal nanocrystal synthesis, which is compelling because they contain polyhedral VO_n ($n = 4, 5, 6$) units that are often also present in the multi-metal oxides of interest. First, we discovered that a commercial tetraalkylammonium halide phase transfer reagent extracts aqueous metavanadate ions into organic solvent, conferring solubility to the resulting polyoxovanadates required for nanocrystal synthesis. We then studied the thermal decomposition of an iron oleate complex mixed with a phase-transferred polyoxovanadate precursor, which yielded previously inaccessible colloidal ternary oxide nanocrystals in high yield, including triclinic FeVO_4 and spinel-type vanadium-doped magnetite ($\text{Fe}_{3-x}\text{V}_x\text{O}_4$) phases. The crystal structure, composition, and morphology of the nanocrystals, which were characterized using X-ray diffraction, Raman scattering, X-ray photoelectron spectroscopy, and transmission electron microscopy, were found to depend strongly on the iron-to-vanadium precursor ratio. The magnetic properties of these colloidal nanocrystals correlated strongly to the phase of vanadium iron oxide, as FeVO_4 displayed antiferromagnetic behavior and a Néel temperature of 21 K, while $\text{Fe}_{3-x}\text{V}_x\text{O}_4$ showed a superparamagnetic-like response with a ferrimagnetic blocking temperature at 162 K. The emergence of polyoxovanadates as precursors to ternary metal oxide nanocrystals that contain vanadium is a significant synthetic advance that may be extensible to other important multi-metal oxide systems.



INTRODUCTION

Multi-metal oxides that contain vanadium are attractive materials for a broad range of applications. A significant number of ternary metal vanadates, for example, have been identified as promising photoanodes for sunlight-driven water splitting in photoelectrochemical cells, a pathway to solar energy storage in the form of chemical fuels.^{1–4} Spinel vanadates of the type MV_2O_4 ($M = \text{Mn, Fe, Co}$) are another example, exhibiting complex magnetic and electronic exchange interactions that are intriguing for data storage and sensing applications.^{5–8} Along similar lines, vanadate compounds $\text{M}_3\text{V}_2\text{O}_8$ ($M = \text{Mn, Co, Ni, Cu, Zn}$) are important platforms for understanding geometrically frustrated magnetism, and in some cases are multiferroic.^{9–11} Cobalt vanadate compounds are recognized as heterogeneous catalysts, especially for oxygen electrochemistry.^{12,13} As broad interest in multi-metal oxides grows, synthetic routes to those that contain vanadium are urgently needed.

Dimensionality is an important variable for many applications of oxide materials. For example, short carrier

diffusion lengths in ternary metal vanadates limit the performance of photoelectrochemical cells by promoting charge recombination. Nanostructures with dimensions that are commensurate with the carrier diffusion length can increase the fraction of photogenerated holes that reach the semiconductor surface.⁴ Improved charge extraction has been observed for nanostructured BiVO_4 , $\gamma\text{-Cu}_3\text{V}_2\text{O}_8$, FeVO_4 , and related photoanode materials.^{4,14–16} Nanoscale size- and shape-engineering also exposes the under-coordinated surface sites that are requisite for heterogeneous catalysts,¹⁷ and influences the domain sizes and anisotropic effects that control magnetism.¹⁸ Accordingly, high surface area, nanostructured, vanadate films have been prepared in many creative ways,

Received: September 29, 2021

Revised: March 14, 2022

Published: March 31, 2022



including electrochemical deposition,^{14,19,20} solution-phase conversion of a nanostructured template,^{21,22} the sol–gel method,²³ and by high-temperature ball milling.²⁴ Precipitation and hydrothermal reactions have afforded free-standing vanadate nanocrystallites that have either been processed into films of connected particles or finely dispersed for catalysis.^{13,25}

The technological promise of dimensionally controlled, multi-metal oxides of vanadium indicates that colloidal nanocrystals (NCs) of those compounds are valuable targets for synthesis. NCs are dimensionally controlled fragments of inorganic solids, with properties that are often strongly dependent on size. Exquisite control over NC morphology, uniformity, and crystallinity can be achieved during synthesis, and NCs can be solution-processed into ordered superlattices and films that function as the active components of devices and catalysts.^{26,27} Opportunities exist for post-synthetic chemical transformation of the NC core and surface,^{28–30} and metastable phases with properties different from the bulk solids often result from surface effects and the relatively low temperatures used for NC synthesis.^{31,32}

Few examples of colloidal NCs contain the element vanadium. Cheon and co-workers demonstrated that V_2O_5 nanorods could be prepared using vanadium(V) oxychloride ($VOCl_3$) as a precursor.³³ More recently, Schaak and co-workers prepared colloidal VO_2 nanostructures, which undergo a metal-to-insulator transition near room temperature, using vanadyl(IV) sulfate ($VOSO_4$) and ZnO nanoparticles as a sacrificial template.³⁴ Acetylacetonate and carboxylate compounds are the most common precursors for late binary and ternary $3d$ metal oxides, but the vanadyl(IV) acetylacetonate [$VO(acac)_2$] and vanadium(III) acetylacetonate [$V(acac)_3$] analogues have not been used as productively to incorporate vanadium into NCs, with a small number of notable exceptions. Milliron and co-workers used $VO(acac)_2$ to prepare V_2O_3 NCs with a metastable bixbyite structure in the 5–30 nm diameter range.³⁵ Additionally, Buonsanti and co-workers used $VO(acac)_2$ to generate cube-shaped Cu_3VS_4 NCs with edge lengths of 10–20 nm. In the latter study, a mixture of amorphous V-containing nanoparticles, Cu_2S , and CuS were generated *in situ* and subsequently underwent solid–solid diffusion to make Cu_3VS_4 cubes.³⁶ $VO(acac)_2$ has also been reacted under hydrothermal conditions to make VO_2 nanostructures in several reports.^{37–39} While impressive morphology and phase control have been demonstrated using these hydrothermal reactions, the tendency of this approach is to produce nanostructures with somewhat larger dimensions than is achievable using surfactant-assisted colloidal synthesis, and consequently the colloidal stability required for solution processing and assembly is typically absent. We attribute the lack of protocols for incorporating vanadium into NCs to a dearth of molecular vanadium precursors. The chemistry of metal acetylacetonates and carboxylates that continues to mature for late $3d$ oxide NC systems is not portable to ternary or multinary oxides of vanadium, and innovations in this area are sorely needed.

Here, we introduce polyoxovanadate (POV) anions as precursors to multi-metal oxide NCs that contain vanadium. Unlike the commonly used acetylacetonate and carboxylate NC precursors for metal oxides, which release oxygen atoms *via* scission of a C–O bond, POVs are comprised of either corner- or edge-sharing VO_n ($n = 4, 5, 6$) polyhedra that resemble structural fragments of the target metal oxides.^{40–42}

For example, $BiVO_4$, $\gamma-Cu_3V_2O_8$, $FeVO_4$, and the Kagome staircase compounds $M_3V_2O_8$ all feature a sublattice of VO_4 structural units. The so-called metavanadate (VO_3^-) clusters $V_2O_7^{4-}$, $V_3O_9^{3-}$, $V_4O_{12}^{4-}$, and others are also constructed of corner-sharing VO_4 tetrahedra, which suggests that they may be ideal vanadium precursors for those targets (Figure 1). POVs may be considered compositionally and structurally “ready” for incorporation into a metal–vanadium–oxygen lattice.

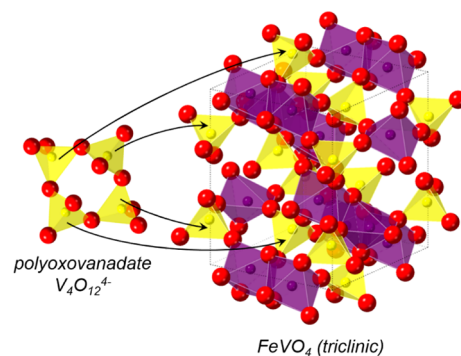


Figure 1. Crystal structure of triclinic $FeVO_4$ is shown on the right, composed of purple FeO_5 and FeO_6 polyhedral units linked by yellow VO_4 tetrahedral units. The cyclic polyoxovanadate anion, $V_4O_{12}^{4-}$, a representative POV, is shown to the left. The figure is intended to highlight the yellow VO_4 tetrahedral units that are common to the POV and the ternary metal oxide. The arrows represent insertion of VO_4 into the multi-metal oxide lattice, a pathway by which vanadium may be incorporated into $FeVO_4$ and other multi-metal oxides of interest.

First, we report a significant development in the methodology for colloidal metal oxide NC synthesis. A tetraalkylammonium halide phase transfer reagent is employed to extract aqueous POVs into organic solvent, conferring solubility to the POVs in liquids that are compatible with our NC synthesis. The extraction is similar to that reported by Do and co-workers for VO_4^{3-} ions during the solvothermal preparation of rare earth orthovanadate NCs.⁴³ Phase transfer is an underutilized strategy for obtaining NC precursors that may be useful for a broad range of polyoxometalates and other ions. We then studied the thermal decomposition of a fatty acid salt $Fe(III)$ *cis*-9-octadecanoate [$Fe(OL)_3$] mixed with a controlled molar ratio of POV precursor, which yielded colloidal ternary oxide NCs including triclinic $FeVO_4$ and spinel-type vanadium-doped magnetite ($Fe_{3-x}V_xO_4$, Figure S1). Although numerous routes to bulk and thin films of these compounds are available, the phases are challenging to access as well-controlled colloidal NCs. $FeVO_4$ is a particularly high-profile synthetic target because it is a multiferroic semiconductor being considered for diverse green technologies, including photoelectrochemical water splitting.^{44–46} The emergence of POVs as precursors to ternary metal oxide NCs that contain vanadium is a significant expansion of synthetic capabilities in the field of nanoscience, and may be extensible to other multi-metal oxide systems.

EXPERIMENTAL SECTION

Materials. All chemicals were used as received. Iron(III) chloride hexahydrate ($FeCl_3 \cdot 6H_2O$, 98%), 1-octadecene (ODE, tech. 90%), oleic acid (OLAC, tech. 90%), Aliquat 336 (AQ336), and potassium metavanadate (KVO_3 , 99.9%, –200 mesh) were purchased from Alfa

Aesar. Sodium oleate was purchased from TCI America. All syntheses were carried out under Ar using standard Schlenk techniques, and work-ups were performed in air. An Fe(OL)₃ complex was prepared using a published procedure⁴⁷ and stored as 0.3 M solutions in ODE. Fe₃O₄ NCs (15 nm) were purchased from Ocean NanoTech.

Organic Extraction of Aqueous Metavanadate Ions and Analysis. Aqueous KVO₃ (0.050 M) and AQ336 (0.050 M) in chloroform (CHCl₃) were rapidly mixed to facilitate phase transfer. In a typical experiment, 690 mg of KVO₃ was dissolved in 100 mL of 18 MΩ purified water using either sonication or immersion in a 60 °C water bath (method of dissolution does not affect result). An amount of 2.02 g of AQ336 was dissolved in 100 mL of CHCl₃, the CHCl₃ solution was layered with the KVO₃ solution, and the mixture was stirred vigorously for 30–40 min. The aqueous and CHCl₃ layers were separated, with the CHCl₃ layer being used to prepare the POV precursor stock solution, hereafter denoted as AQ336⁺VO₃⁻, and the aqueous solution was retained for analysis. The CHCl₃ was removed by rotary evaporation, yielding a viscous, pale yellow oil that was dissolved in sufficient ODE to make a 0.3 M stock solution. Phase transfer efficiency was analyzed using both UV–vis spectroscopy (Agilent 8453 spectrometer) and Cl⁻ ion selective potentiometry (Thermoscientific Orion combination chloride ion-selective electrode, ISE). A calibration curve was generated from absorption of KVO₃ solutions with known concentrations at 260 nm (Figure S2) and used to determine the aqueous VO₃⁻ remaining after extraction. The UV–vis spectra were corroborated by measuring the transfer of Cl⁻ ions from the AQ336 solution to the aqueous layer using Cl⁻ ion-selective potentiometry. The Cl⁻ ISE was calibrated before each measurement using 0.1 M NaCl standard (Thermo Scientific), and an ionic strength adjuster (Thermo Scientific) was added to each standard and sample.

Synthesis of Fe–V–O Nanocrystals. Fe(OL)₃ (0.3 M), AQ336⁺VO₃⁻ (0.3 M), and ODE were mixed in a 25 mL round-bottom flask, targeting Fe:V molar ratios of 1:1, 2:1, 4:1, and 8:1, an Fe(OL)₃ concentration of 0.16 M, and a total reaction volume between 6 and 8 mL (Table S1). The flasks were fitted with a reflux condenser and temperature probe, sealed, and degassed at 80–100 °C under vacuum for 30 min. The reaction mixture was then heated under Ar to the reflux temperature, 310–320 °C, at a ramp rate of 3.0–3.5 °C min⁻¹. The reaction was subsequently cooled after 30 min of heating, and 2-propanol was added to precipitate the nanocrystals. Centrifugation (9000 rpm or 942 rad/s) was applied to collect the black/brown precipitate, and several redispersion/centrifugation cycles in hexanes/ethanol were used to purify the product. The purified NC product was stored in 5 mL of a solution made by dissolving 0.250 mL of oleic acid and 0.250 mL of oleylamine in 40 mL of hexanes, which produced black/brown dispersions that were colloidally stable for months (Figure S3). When appropriate, size-selective precipitation was conducted. Large particles were selectively collected by iteratively increasing the solvent:antisolvent ratio from 1:1 to 3:2 to 2:1 and discarding the decanted brown/tan supernatant after each iteration. After the resulting supernatant appeared to be nearly clear, the precipitate was redispersed in pure hexanes. Likewise, small particles were selectively obtained by repeated centrifugation using a 2:1 solvent:antisolvent ratio and discarding any resulting dark brown precipitate. When no further material would precipitate, the resulting brown supernatant solution was collected with excess ethanol and redispersed in hexanes.

Control Reactions Excluding Fe(OL)₃ or AQ336⁺VO₃⁻. We reacted either Fe(OL)₃ or AQ336⁺VO₃⁻, excluding one or the other reactant, under concentration and heating conditions identical to those described for synthesis of Fe–V–O NCs. In the first control experiment, a degassed 8 mL volume of 0.16 M Fe(OL)₃ in ODE was slowly heated under Ar to reflux, the red-brown solution gradually turning darker brown/black in color with increasing temperature. After 30 min of heating at the highest achievable temperature (≈318 °C), the mixture was cooled, and several redispersion/centrifugation cycles in hexanes/ethanol were used to purify the NC product.

Using reaction conditions identical to that described for Fe–V–O NCs, 0.16 M AQ336⁺VO₃⁻ in ODE was also degassed and reacted in the absence of Fe(OL)₃. The yellow AQ336⁺VO₃⁻ solution gradually

turned brown as the temperature was increased, turning black at 170 °C. At 210 °C, a solid black precipitate was observed. After 30 min of heating at the highest achievable temperature (≈310 °C), the reaction mixture was cooled, and the black precipitate was purified using several cycles of centrifugation and redispersion in hexanes/ethanol.

Nanocrystal Characterization. Powder X-ray diffraction (XRD) data were collected using a Bruker D8 Discover X-ray diffractometer equipped with Cu Kα radiation. Transmission electron microscopy (TEM) images were obtained from a Phillips EM-400 operating at an acceleration voltage of 120 kV. High-resolution TEM (HRTEM) imaging and high-angle annular dark-field scanning TEM (HAADF-STEM) coupled with energy-dispersive X-ray spectroscopy (EDXS) were conducted using an FEI Titan 80-300 operating at 300 kV. Samples were prepared by suspending the washed nanocrystals in hexanes and drop-casting onto Formvar-coated copper TEM grids. The Raman spectra of NCs drop-cast on Si were collected using a Renishaw inVia system (1800 grooves/mm grating, 1" CCD detector), with 633 nm HeNe excitation in a 180° back-scattering configuration through a 50x objective (Leica). Typical collection parameters were 180 s at 2.0 mW power. The X-ray photoelectron spectra (XPS) were obtained using a Kratos Axis Ultra system with a monochromatic Al Kα excitation source operating at 15 kV and 10 mA. The pass energy used was 20 eV, and data analysis was conducted with Shirley backgrounds using CasaXPS. Optical band gaps were determined using the Tauc method from the absorbance spectra measured with a Perkin Elmer Lambda 25 spectrophotometer. Samples were drop-cast onto quartz substrates. The X-ray fluorescence (XRF) spectra were collected using a Bruker M4 Tornado micro-XRF spectrometer equipped with a Rh source and a Si detector. Magnetic characterization was performed on dried powders using the vibrating sample magnetometry option of a Quantum Design Dynacool Physical Property Measurement System.

RESULTS AND DISCUSSION

Extraction of Aqueous Metavanadate Ions into Organic Solvent. Common sources of VO₃⁻ ion (e.g., KVO₃, NH₄VO₃), which undergo speciation into POVs when dissolved in water, are not compatible with the hydrophobic solvents and surfactants commonly used for NC synthesis. Phase transfer of aqueous VO₃⁻, driven by ion-pairing with organic-soluble cations, is a yet underexplored strategy that we are developing to circumvent these limitations. A commercially available phase transfer agent, Aliquat 336 (AQ336), composed primarily of methyltriocetylammmonium chloride, extracts aqueous POVs into organic solvent and confers solubility to the POVs in high-boiling solvents that are typical of NC preparation. AQ336 extracts metavanadate ions from aqueous KVO₃ solution into chloroform (CHCl₃) at approximately 60% efficiency. In a typical process for preparing stock solutions of the POV precursor, hereafter denoted as AQ336⁺VO₃⁻, 100 mL of 0.050 M aqueous KVO₃ was layered with 100 mL of 0.050 M AQ336 in CHCl₃ and stirred vigorously for 30 min. We measured the decrease in absorbance at 260 nm, corresponding to extraction of VO₃⁻ from the aqueous phase, and a typical concentration after extraction was 0.0185 M (37% remaining in the aqueous layer, see Figure S2 for the calibration plot). The concomitant transfer of Cl⁻ ions from the AQ336 solution to the aqueous layer was also measured using Cl⁻ ion-selective potentiometry. We routinely obtained excellent agreement between the two measures of phase transfer efficiency, within 3% or less. The agreement between the VO₃⁻ absorbance and Cl⁻ ion measurements enabled us to generate stock solutions in 1-octadecene (ODE) with reasonably well-assigned AQ336⁺VO₃⁻ concentrations, typically targeting 0.30 M. More efficient phase transfer was observed when we used

AQ336:KVO₃ ratios greater than 1. Near quantitative ($\approx 97\%$) phase transfer was observed for extractions when the AQ336:KVO₃ ratio was 2. All AQ336:KVO₃ ratios we used for extraction resulted in precursor stock solutions containing excess AQ336 and thus excess Cl⁻ ions. Halide ions are known to influence nucleation and growth processes during NC synthesis,⁴⁸ so we sought to minimize the excess AQ336 by using an AQ336:KVO₃ ratio of 1 during extraction for all NC precursor solutions.

Metavanadate ions undergo complex concentration and pH-dependent speciation into POVs when dissolved in water. The structure of these anions has been studied extensively and summarized recently by Rompel and Gumerova.⁴⁹ It is reasonable to hypothesize, based on previous reports, that the POVs in our AQ336⁺VO₃⁻ precursor are dominantly cyclic V₄O₁₂⁴⁻ ions (Figure 1). The linear tetranuclear analogue (V₄O₁₃⁶⁻) has neither been observed in organic solutions nor isolated in the solid state, and the trinuclear, cyclic, V₃O₉³⁻ ion dominates at lower concentrations than those used here.^{50,51} Nevertheless, our NC precursor may contain a mixture of POVs, and the presence of V₄O₁₃⁶⁻, V₃O₉³⁻, protonated analogues,⁵² and others⁴⁹ cannot be ruled out. The POVs that our AQ336⁺VO₃⁻ precursor contains are constructed of the corner-sharing VO₄ structural units of interest.

Nanocrystal Synthesis Using Fe(OL)₃ and AQ336⁺VO₃⁻ Precursors. Fe(OL)₃ was combined with AQ336⁺VO₃⁻ in either 1:1, 2:1, 4:1, or 8:1 Fe:V molar ratio, and heated to the reflux temperature of ODE solvent (310–320 °C) at a controlled ramp rate of 3.0–3.5 °C min⁻¹. The solution color changed gradually from dark red to brown to black in the temperature window 80–200 °C, which is similar to that observed when preparing Fe₃O₄ NCs using Fe(OL)₃ as a precursor.⁴⁷ Representative powder X-ray diffraction (XRD) patterns for each NC sample are shown in Figure 2, along with simulated patterns for Fe₃O₄ (PDF 04-007-9093) and Fe₂VO₄ (PDF 04-006-8198), which both have the inverse spinel structure. With the exception of a very small shift to larger d-

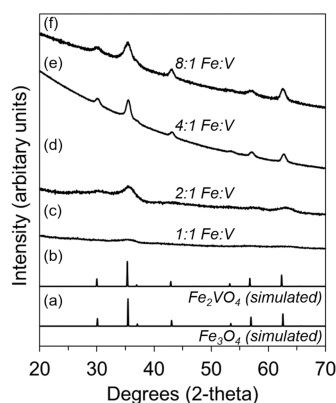


Figure 2. Simulated powder XRD patterns in (a) and (b) correspond to spinel-type Fe₃O₄ and Fe₂VO₄, which show that the unit cell dimensions for the two compounds are nearly identical. The experimental XRD patterns in (c–f) represent NC samples that were prepared with different Fe:V precursor ratios under otherwise identical conditions. Weak diffraction from the 1:1 Fe:V sample in (c) indicates particles that are either amorphous or small in size. The intensity and distinguishability of the reflections increase as the Fe:V ratio rises, with peak positions and intensities that match the simulated spinel patterns. (Fe₂VO₄, PDF 04-006-8198; Fe₃O₄, PDF 04-007-9093).

spacings for Fe₂VO₄ (e.g. $d_{311} = 2.540$ vs 2.531 Å), the two simulated patterns are indistinguishable. Each sample has broad reflections indicative of nanometer-sized crystallites, with peak positions and intensities that correlate well with the simulated patterns. Extremely broad, weak, reflections are observed for the 1:1 Fe:V sample, suggesting that it contains either mostly amorphous particles or particles that are too small to produce significant diffraction. The diffraction peaks became more intense as the Fe:V precursor ratio was increased, with enhanced distinguishability and clearer correlation to each simulated peak that suggests increasing crystallite size.

A clear trend can be observed in the transmission electron microscopy (TEM) images of the 2:1, 4:1, and 8:1 Fe:V samples shown in Figure 3a–c. Each sample contains a bimodal distribution of nanoparticle sizes. For example, Figure 3a is representative of samples prepared using a 2:1 Fe:V precursor ratio, showing smaller, irregularly shaped particles with an average diameter of $5.7 \text{ nm} \pm 1.4 \text{ nm}$ ($n = 150$) mixed with a low population of larger, more spherical particles having an average diameter of $19.4 \text{ nm} \pm 5.6 \text{ nm}$ ($n = 55$). The number of larger nanoparticles, relative to the smaller particles increases with the Fe:V precursor ratio. The 2:1 Fe:V sample contains relatively few of the larger particles (Figure 3a), and the 8:1 Fe:V sample contains the highest concentration of the larger particles (Figure 3c). The smaller particles in the 8:1 Fe:V sample have an average diameter of $3.9 \text{ nm} \pm 0.8 \text{ nm}$ ($n = 150$), while the larger particles are $13.5 \text{ nm} \pm 1.9 \text{ nm}$ ($n = 150$). The correlation between the trends observed by XRD and in the TEM images is intriguing. The intensity and distinguishability of the diffraction peaks increased with the increasing Fe:V precursor ratio, as did the relative number of larger particles observable by TEM, which suggests that the larger particles are responsible for the more intense diffraction. The relatively larger particles observed by TEM have a crystal structure that is identifiably spinel type, based on matching to the simulated XRD patterns. Furthermore, TEM images of the samples prepared using a 1:1 Fe:V precursor ratio (Figure S4) indicate the presence of very few nanoparticles outside of the range $5.2 \text{ nm} \pm 0.8 \text{ nm}$ ($n = 150$), which produced the weakest, broadest diffraction peaks we observed in our samples.

Size-selective precipitation enabled us to significantly enrich the samples in either the relatively smaller or larger nanoparticles. For example, we removed most of the larger nanoparticles from the 2:1 Fe:V sample by adding a small amount of antisolvent to induce precipitation followed by centrifugation. The TEM image in Figure 3d shows a substantial area of the sample, free of the larger particles, dominated by the smaller particles. High-resolution transmission electron microscopy (HRTEM) images in Figure S5 reveal that the sample is crystalline, as evidenced by observable lattice planes in each nanoparticle. Figure 3e shows an 8:1 Fe:V sample that was enriched in larger nanoparticles using iterative size-selective precipitation, and HRTEM (inset and Figure S6) indicates that many of the NCs are single crystalline. Larger-area TEM images of each size-selectively treated sample are shown in Figure S7. The enrichment we observed allowed us to confidently assign subsequent characterizations to either the smaller or larger NCs at the ensemble level.

Spectral Characterization and Phase Identification. Raman scattering from phonons in the 200–1000 cm⁻¹ range

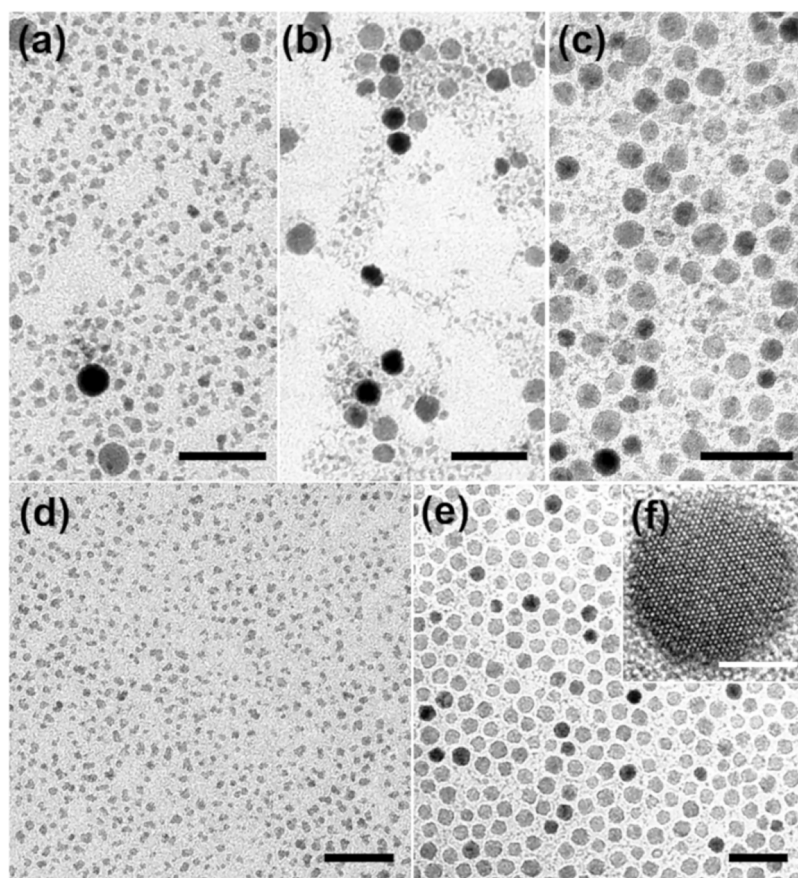


Figure 3. TEM images in the upper panels represent NC samples prepared using (a) 2:1, (b) 4:1, and (c) 8:1 Fe:V precursor ratios, respectively. Each sample has a size distribution that is bimodal, consisting of relatively small and large nanoparticles. The ratio of large-to-small nanoparticles increases with an increasing Fe:V precursor ratio. The 2:1 Fe:V sample in (a) was subject to size-selective precipitation, and the small nanoparticle fraction is shown in (d). Size-selective precipitation was also performed on the 8:1 Fe:V sample shown in (c), and a representative TEM image of the large nanoparticle fraction is shown in (e). The representative HRTEM image in (f) indicates that the larger nanocrystals are single crystalline. The scale bars in (a–e) are each 50 nm, and the scale bar in (f) is 5 nm.

indicated the presence of two different crystal phases in each of the NC samples prior to size-selective precipitation. The Raman spectra for samples as-synthesized with 2:1 and 8:1 Fe:V precursor ratios are shown in Figures 4a,b, respectively. The phonon modes marked with asterisks (*) appear in both samples but at higher relative intensity in the 8:1 Fe:V sample than in the 2:1 Fe:V sample. These phonon modes are similar to those expected for hematite (α - Fe_2O_3),⁵³ which likely arise from laser heating-induced oxidation of the larger, spinel-type nanocrystals while being irradiated in air.⁵⁴ Indeed, commercial Fe_3O_4 magnetic nanoparticles (Ocean NanoTech) display a nearly identical hematite-like Raman spectrum using the same measurement conditions (Figure S8). Unfortunately, lowering the laser power resulted in negligible Raman scattering detected in our as-synthesized samples. The phonon modes marked with vertical lines (l) appear weak in the 8:1 Fe:V sample, in which TEM indicated was rich in larger NCs, but much more prominently in the 2:1 Fe:V sample consisting mostly of smaller NCs. These phonon modes are consistent with those expected for triclinic FeVO_4 .^{55,56} The eight peaks in the relatively high frequency 600–1000 cm^{-1} range are due to Fe–V–O stretching modes, and the three peaks in the 300–500 cm^{-1} range are combinations of high-frequency stretching modes with low-frequency torsional modes. The Raman spectrum of the 1:1 sample appeared similar (Figure S9a), which was consistent with TEM images showing that it is

comprised primarily of smaller particles. The Raman spectrum of the as-synthesized 4:1 sample confirmed this trend, as significant intensities were detected due to both the $\text{Fe}_{3-x}\text{V}_x\text{O}_4$ and FeVO_4 phonon modes (Figure S9b), and TEM analysis indicated that it is a true mixture of both larger and smaller particles.

We observed that drop-cast films of as-synthesized samples rich in larger NCs generate the Raman spectra with phonon modes that are primarily attributable to $\text{Fe}_{3-x}\text{V}_x\text{O}_4$, while the spectra obtained from smaller NCs have prominent modes that can be assigned to FeVO_4 . To confirm these trends, we also studied samples that were subjected to size-selective enrichment (Figure S10). For example, the enriched sample prepared with a 2:1 Fe:V precursor ratio consisted mostly of smaller, 5.7 nm nanoparticles. The Raman spectrum collected from the precipitate removed from this sample was rich in the lower-frequency modes attributed to $\text{Fe}_{3-x}\text{V}_x\text{O}_4$, while the remaining portion showed an intensity increase, relative to the as-synthesized mixture, in the higher-frequency FeVO_4 modes. Conversely, the product prepared with an 8:1 Fe:V precursor ratio contained mostly larger nanoparticles, with an average diameter of 13.5 nm. The supernatant liquid removed during size-selective treatment produced Raman scattering rich in FeVO_4 modes, while the spectrum of the remaining sample showed a negligible intensity of these same modes. Importantly, we found that the Raman spectra could be

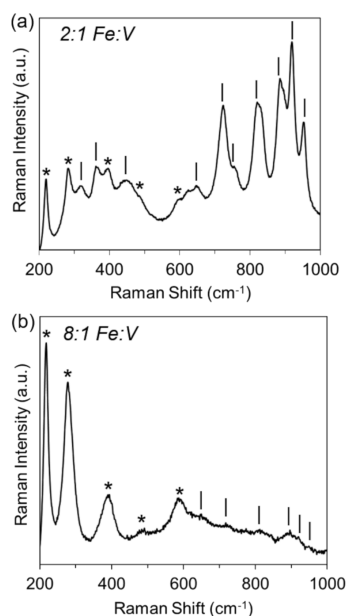


Figure 4. Raman spectra, using 633 nm excitation, of drop-cast NC samples prepared using (a) 2:1 Fe:V and (b) 8:1 Fe:V precursor ratios, highlighting the distinguishably different set of intense phonon modes present in the two samples. The peaks marked with asterisks (*) are more intense in the 8:1 Fe:V sample and consistent with α - Fe_2O_3 (hematite), likely observed due to laser-induced heating of the larger, spinel-type NCs in air. The peaks marked with vertical lines (|) are consistent with triclinic FeVO_4 and are more intense in the 2:1 sample.

collected from the enriched 13.5 nm NCs at low excitation power (0.3 mW), and the resulting spectrum matched well to previous reports of transition metal-doped magnetite (Figure S10e).⁵⁷ This confirms that our synthetic procedure generates spinel-type doped iron oxides, which are subsequently laser heat oxidized to hexagonal hematite at the fluences necessary to produce significant scattering in the as-synthesized samples.

Samples subjected to size-selective enrichment were also analyzed using XPS, and the observed binding energies are in good agreement with literature values for vanadium and iron oxides.^{58,59} Figure 5a,b shows the V 2p and Fe 2p regions for an enriched 2:1 Fe:V sample (5.7 nm NCs). The +5 and +4 oxidation states of vanadium are present, as shown in the V 2p spectrum, and integration of the fitted peaks indicated a substantially larger contribution from V^{5+} (73% V^{5+} , 27% V^{4+}). The Fe 2p spectrum indicates that the oxidation state for Fe is dominantly +3 (91%), with minor contributions from Fe^{2+} (9%). Collectively, the larger contributions from V^{5+} and Fe^{3+} suggest that the dominant phase resulting from a 2:1 Fe:V precursor ratio is triclinic FeVO_4 , in agreement with the Raman spectrum in Figure 4a. The relatively minor presence of reduced species V^{4+} and Fe^{2+} can be attributed to the small population of larger particles either remaining or are present at the 5.7 nm particle surface, coordinated by oleate ligands (-1) instead of O^{2-} . The V 2p and Fe 2p spectra for the enriched 8:1 Fe:V sample (13.5 nm), shown in Figure 5c,d, have a different distribution of oxidation states. The fitted contributions for vanadium in the 13.5 nm nanocrystals include +5 (25%), +4 (53%), and +3 (22%), with the largest contribution coming from the +4 state. Comparable intensity contributions from both Fe^{3+} (52%) and Fe^{2+} (48%) are seen in fitting the Fe 2p spectrum, in contrast to the dominantly Fe^{3+} 5.7 nm

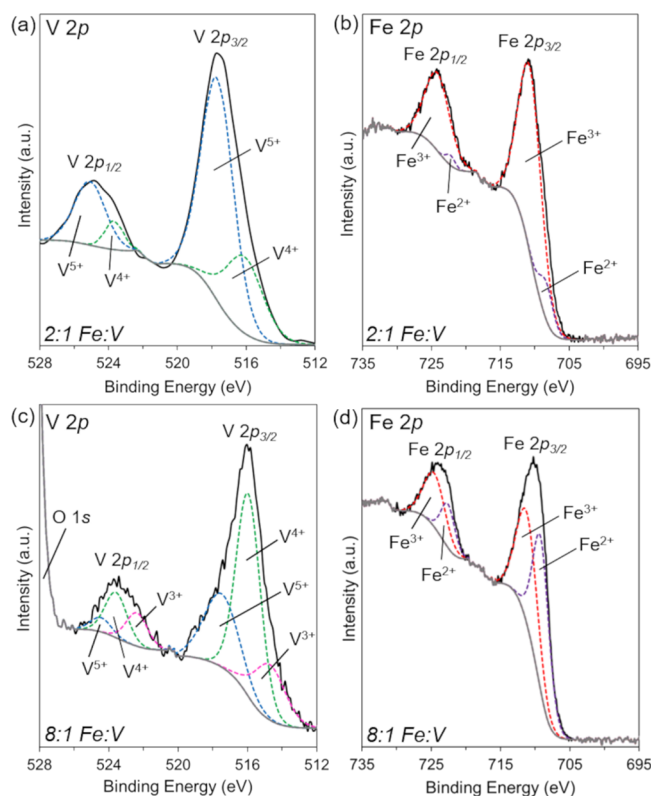


Figure 5. XPS spectra of NC samples prepared using (a, b) 2:1 Fe:V and (c, d) 8:1 Fe:V precursor ratios, highlighting the different oxidation state distributions present in each sample. The (a) V 2p and (b) Fe 2p spectra show the largest contributions to the overall fit from V^{5+} (73%) and Fe^{3+} (91%) with relatively minor intensities from V^{4+} (27%) and Fe^{2+} (9%), which is consistent with FeVO_4 . The (c) V 2p spectrum for the spinel, 8:1 Fe:V sample, has an oxidation state distribution that includes V^{5+} (25%), V^{4+} (53%), and V^{3+} (22%). The (d) Fe 2p spectrum for the 8:1 Fe:V sample indicates comparable contributions to the overall fit from Fe^{3+} (52%) and Fe^{2+} (48%).

particles. Several stoichiometric combinations of the V and Fe oxidation states, observed in the enriched 8:1 Fe:V XPS data, are consistent with the spinel structure we have proposed for the larger NCs, including $\text{Fe}^{\text{II}}_2\text{V}^{\text{IV}}\text{O}_4$ and $\text{Fe}^{\text{II}}\text{Fe}^{\text{III}}\text{V}^{\text{III}}\text{O}_4$. Deviations from these formulae are permitted by the presence of bulk vacancies and surface defects.

We also conducted high-angle annular dark-field scanning TEM coupled with energy-dispersive X-ray spectroscopy (HAADF-STEM-EDXS) on our enriched samples to elucidate the elemental ratio of individual FeVO_4 and $\text{Fe}_{3-x}\text{V}_x\text{O}_4$ NCs (Figure 6a,b and Figures S11 and S12). Spot scans of the 5.7 nm NCs were found to be vanadium-deficient, relative to pristine FeVO_4 , with an Fe:V ratio of 59:41. Similar non-stoichiometry has been observed in the Fe–V–O system by Ludwig and co-workers,⁶⁰ where triclinic FeVO_4 was the dominant phase present in magnetron cosputtered films with compositions ranging from 42 to 66 atomic % Fe. Phases with approximately the same range of vanadium deficiency have also been reported for the related photoanode material BiVO_4 , without a change to the monoclinic crystal structure.^{61,62} The average vanadium doping level in the spinel magnetite 13.5 nm NCs was determined by EDXS to be approximately $\text{Fe}_{2.8}\text{V}_{0.2}\text{O}_4$. Although some particle-to-particle variation in stoichiometry was observed, the $\pm 5\%$ deviation is consistent with error associated with the EDXS technique. STEM-EDXS

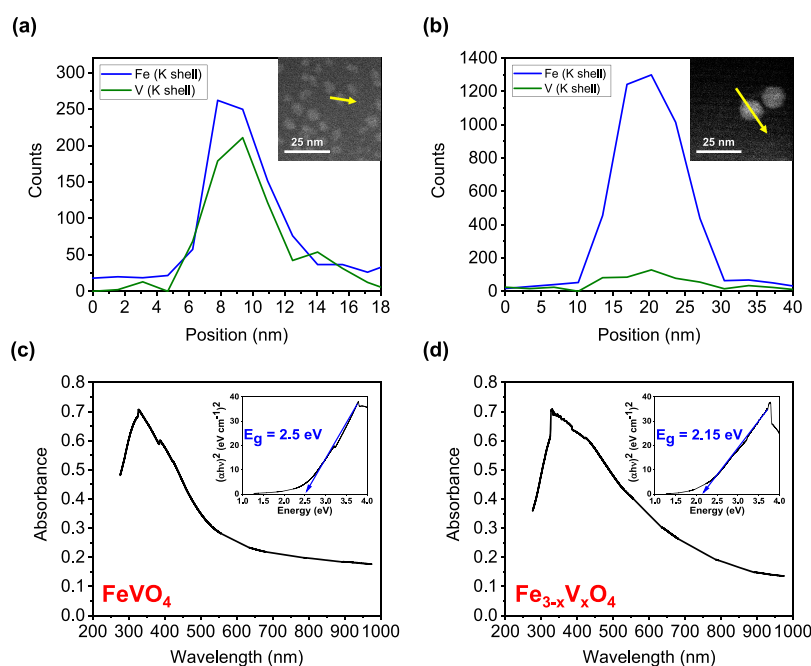


Figure 6. STEM-EDXS line scans of individual (a) 5.7 nm FeVO_4 NCs and (b) 13.5 $\text{Fe}_{3-x}\text{V}_x\text{O}_4$ NCs (inset: HAADF-STEM images of the scanned NCs), indicating a slightly iron-rich stoichiometry of triclinic FeVO_4 NCs and a vanadium doping level of $x \approx 0.2$ in the spinel ferrite NCs. The absorbance spectra and corresponding Tauc plots (inset) revealed optical band gap measurements of (c) 2.5 eV for enriched 5.7 nm FeVO_4 NCs and (d) 2.15 eV for enriched 13.5 nm $\text{Fe}_{3-x}\text{V}_x\text{O}_4$ NCs.

elemental line scans and mappings revealed a generally uniform distribution of Fe and V throughout the particle, with no core–shell or multi-domain architectures detected. Taken together, the XRD, TEM, Raman, XPS, and STEM-EDXS data definitively conclude that the larger colloidal NCs have a spinel structure that may be expected from solid solution $\text{Fe}_{3-x}\text{V}_x\text{O}_4$ ($x \approx 0.2$) and the smaller NCs are vanadium-deficient triclinic FeVO_4 .

Control Reactions Excluding $\text{Fe}(\text{OL})_3$ or $\text{AQ336}^+\text{VO}_3^-$.

To generate further insights into our synthetic protocol, we reacted only $\text{Fe}(\text{OL})_3$ or $\text{AQ336}^+\text{VO}_3^-$, excluding one or the other reagent, under conditions identical to those described for synthesis of Fe–V–O NCs. For the reaction including only $\text{Fe}(\text{OL})_3$, the XRD data presented in Figure S13a indicate the presence of both inverse spinel Fe_3O_4 and wüstite Fe_{1-x}O phases in the NC product. Although synthesis of phase-pure Fe_3O_4 NCs has been reported using thermal decomposition of $\text{Fe}(\text{OL})_3$,⁴⁷ several other studies indicate that a mixture of iron oxide phases that includes wüstite Fe_{1-x}O is often obtained using this approach.^{63–65} Reproducibility is often poor because the pathways by which metal–carboxylate complexes undergo thermal decomposition are sensitive to subtle structural variations and impurities that arise during precursor synthesis and purification.³² TEM images (Figure S13b) indicate that thermal decomposition of our $\text{Fe}(\text{OL})_3$ precursor generates uniform, spherical NCs ($d = 16.2 \pm 0.7$ nm, $n = 100$), but with a substantial population of core–shell particles indicative of a mixture of phases.

When 0.16 M $\text{AQ336}^+\text{VO}_3^-$ in ODE was reacted in the absence of $\text{Fe}(\text{OL})_3$, an insoluble black precipitate was obtained. The XRD measurements in Figure S14a show that the product is mostly amorphous, with diffuse scattering and weak diffraction peaks that cannot be assigned to any one phase or mixture of phases. Matching of simulated XRD data to our experimental data suggests that a small amount of

orthorhombic V_2O_5 may be present in the sample. The TEM images in Figure S14b are consistent with the XRD results, showing a mixed product with irregular morphology. The Raman spectrum, however, matches phase-pure V_2O_5 (Figure S14c), suggesting that the sample underwent laser-induced crystallization during the measurement.⁶⁶

Optical and Magnetic Properties of Fe–V–O NCs. The solution-phase absorbance spectra of colloidal FeVO_4 and $\text{Fe}_{3-x}\text{V}_x\text{O}_4$ NCs in hexane following size-selective precipitation are presented in Figure S15. Each sample exhibits absorbance throughout the visible region that increases with decreasing wavelength. The solution-phase absorbance of $\text{Fe}_{3-x}\text{V}_x\text{O}_4$ NCs is interesting to compare to what is expected for Fe_3O_4 NCs to observe the effects of vanadium incorporation. The absorbance spectrum of $\text{Fe}_{3-x}\text{V}_x\text{O}_4$ NCs exhibits an absorption onset (730–740 nm) that is blue-shifted compared to what has been observed previously for Fe_3O_4 NCs (775–800 nm).^{67,68} The absorbance spectrum of commercial 15 nm Fe_3O_4 NCs dispersed in water (Figure S16a) is similar to $\text{Fe}_{3-x}\text{V}_x\text{O}_4$ NCs throughout the visible region, but with a lower-energy absorption onset of around 780 nm.

Films of our FeVO_4 and $\text{Fe}_{3-x}\text{V}_x\text{O}_4$ NCs were drop-cast on quartz to measure their optical band gaps using the Tauc method (Figure 6c,d). We found the direct band gap of the FeVO_4 NCs to be 2.5 eV, which is wider than the reported value for bulk and thin-film FeVO_4 (2.1 eV–2.2 eV).⁶⁹ The wider band gap may result from either the presence of vanadium vacancies or from quantum confinement due to the small diameter of the NCs. Both band gap engineering and nanostructuring are recognized as potential ways to augment the already substantial utility of FeVO_4 as a visible light photocatalyst.^{4,70} For our $\text{Fe}_{3-x}\text{V}_x\text{O}_4$, we found that the direct optical band gap is 2.15 eV. It is difficult to compare this to previous results due to a dearth of published vanadium ferrite reports. However, smaller band gaps have been reported for

undoped magnetite NCs measured by Tauc analysis.^{71–73} Indeed, the absorbance spectrum of drop-cast 15 nm Fe₃O₄ (Figure S16b) has an onset of approximately 780 nm (1.6 eV), so we are confident that vanadium doping has a substantial effect on the electronic band structure. We conclude that incorporation of vanadium into the spinel crystal, even in modest amounts, affects the band gap in the visible region and may serve to synthetically tune the optoelectronic properties of these NCs for semiconductor applications.

The magnetic properties of our NCs were investigated using vibrating sample magnetometry. Figure 7a shows the field-

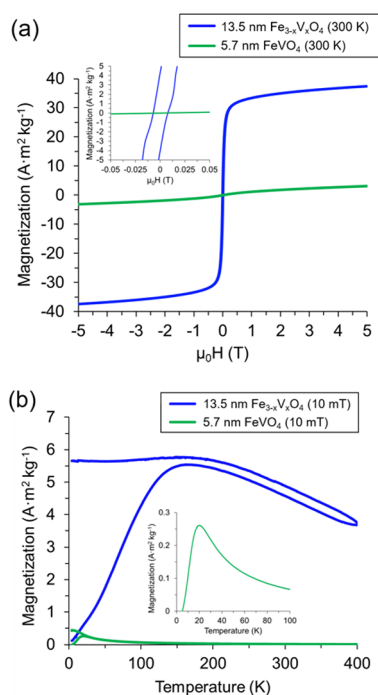


Figure 7. Magnetic properties of enriched NC powders. (a) Field-dependent magnetization at 300 K, indicating that the 13.5 nm Fe_{3-x}V_xO₄ NCs display superparamagnetic-like behavior, with a coercivity of 9 mT, while the 5.7 nm FeVO₄ NCs are paramagnetic. (b) Zero-field cooled and field-cooled magnetization, which reveals a blocking temperature of 162 K for 13.5 nm Fe_{3-x}V_xO₄ and a Néel temperature of 21 K for 5.7 nm FeVO₄.

dependent magnetization collected from powders of particles following size-selective precipitation. The 13.5 nm Fe_{3-x}V_xO₄ sample behaves similarly to Fe₃O₄ of comparable size at 300 K, with a saturation magnetization of 38 A·m² kg⁻¹ and coercivity of 9 mT (inset). As shown in Figure S13a, the saturation magnetization increases steadily with decreasing temperature until around 100 K and the coercivity increases substantially when cooled below 100 K. Both trends are consistent with superparamagnetic-like NCs transitioning from a very soft unblocked state to a harder ferrimagnetic blocked state as thermal energy is removed. Conversely, the DC magnetic response of 5.7 nm FeVO₄ is purely paramagnetic at 300 K, with no detectable coercivity and a mass-normalized magnetization over an order of magnitude lower at a ±5 T applied field.

The temperature-dependent magnetic properties of these two materials at a fixed 10 mT applied field are displayed in Figure 6b. Zero field-cooled (ZFC) and field-cooled (FC) measurements revealed further superparamagnetic-like behav-

ior in the 13.5 nm Fe_{3-x}V_xO₄, with a blocking temperature of 162 K. As seen in Figure S13c, ZFC-FC measurements conducted on powders of commercially available 15 nm Fe₃O₄ indicated a blocking temperature of 144 K, which suggests that vanadium doping into the spinel lattice of these NCs may be responsible for the transition from a blocked to an unblocked state occurring at higher temperature than that of similarly sized undoped Fe₃O₄. Notably, the mass-normalized 10 mT magnetization of our vanadium-doped iron oxide is also nearly 50% higher than its undoped counterpart when in the unblocked state. The magnetic behavior of the 5.7 nm NCs is substantially different, showing very little mass-normalized magnetization until the temperature is cooled below 50 K. Examination of the low-temperature ZFC response (inset) indicates that a peak corresponding to a magnetic ordering temperature occurs at 21 K. This behavior is consistent with previous reports on the magnetic properties of triclinic FeVO₄, which displays an antiferromagnetic ordering Néel temperature ranging from 20 to 22 K.⁷⁴ Collectively, these observed magnetic characteristics strongly corroborate that our reaction system yields two distinct ternary iron–vanadium oxide phases, Fe_{3-x}V_xO₄ and FeVO₄, that we can subsequently separate using size-selective precipitation.

Interpretation of Reaction Pathway. The reaction of the AQ336⁺VO₃⁻ precursor with the Fe(OL)₃ complex generated NCs with a mixture of crystal phases, identified as triclinic FeVO₄, and vanadium-doped, spinel-type, magnetite with the formula Fe_{3-x}V_xO₄. Whether FeVO₄ is present in the product mixture did not depend controllably on the Fe:V precursor ratio. A mixture of FeVO₄ and Fe_{3-x}V_xO₄ phases was observed for all targeted compositions, namely, the 1:1 compound FeVO₄ was generated even when 2:1, 4:1, or 8:1 Fe:V precursor ratios were used. POVs contain tetrahedral, VO₄ units that are often also present in multi-metal oxides. Indeed, triclinic FeVO₄ is built from chains of FeO₅ and FeO₆ polyhedra that are connected by VO₄ tetrahedra with a central V⁵⁺. In contrast, the XPS analysis shows that Fe_{3-x}V_xO₄ contains a mixture of V⁴⁺ and V³⁺, consistent with a previous report where V⁴⁺ and V³⁺ dopants were detected at the surface and in the near-surface bulk of Fe₃O₄.⁷⁵ In FeV₂O₄ and other spinel vanadates, the octahedral sites are occupied by V³⁺.^{5,6} Assuming that V⁴⁺ and V³⁺ are also octahedrally coordinated in the Fe_{3-x}V_xO₄ NCs, the different coordination and oxidation states of vanadium in the spinel and triclinic phases suggest that significantly different reaction conditions may lead to nucleation of one phase or the other. The tetrahedral VO₄ precursor units are likely to facilitate formation of FeVO₄ more rapidly than they do Fe_{3-x}V_xO₄ because they undergo less structural and chemical changes, implying that lower temperatures might be required to nucleate FeVO₄. It is interesting to consider, however, that the VO₄ precursor units might facilitate tetrahedral coordination for vanadium ions that may otherwise prefer octahedral sites in the spinel structure, which is a possible pathway to metastable phases. The oxidation states of Fe and V in FeVO₄ are the same as the Fe³⁺ and V⁵⁺ found in the precursors, but formation of Fe_{3-x}V_xO₄ requires reduction of Fe³⁺ to Fe²⁺ and V⁵⁺ to V⁴⁺ and V³⁺. In addition to iron oxides, the thermal decomposition of the Fe(OL)₃ complex is known to produce side products such as H₂, ketones, and radical hydrocarbon fragments⁷⁶ that are likely responsible for reducing the metal species that nucleate Fe_{3-x}V_xO₄ at elevated temperature.

Our present interpretation of the reaction pathway is that FeVO_4 nucleation overlaps in temperature and competes with the generation of monomer units that lead to the spinel phase. The $\text{AQ336}^+\text{VO}_3^-$ precursor remaining, which is not consumed in the formation of FeVO_4 , generates Fe–V–O monomer units that are incorporated into $\text{Fe}_{3-x}\text{V}_x\text{O}_4$ at the higher temperatures characteristic of $\text{Fe}(\text{OL})_3$ thermolysis ($>300^\circ\text{C}$). Ensemble XRF measurements support this hypothesis (Figure S14). Size-selective separation of samples made with a 4:1 or 8:1 Fe:V precursor ratio leads to samples rich in the spinel-phase product. The 4:1 Fe:V product contained 92% Fe and 8% V ($\text{Fe}_{2.76}\text{V}_{0.24}\text{O}_4$), and the 8:1 Fe:V product contained 95% Fe and 5% V ($\text{Fe}_{2.85}\text{V}_{0.15}\text{O}_4$), suggesting that much of the $\text{AQ336}^+\text{VO}_3^-$ precursor is consumed in the formation of FeVO_4 . The number of oxygen atoms required to form FeVO_4 can be supplied by the VO_4 tetrahedral units in the $\text{AQ336}^+\text{VO}_3^-$ precursor. In order for vanadium to occupy the octahedral sites in $\text{Fe}_{3-x}\text{V}_x\text{O}_4$, coordination of VO_4 by two additional equivalents of oxygen is required, which are likely supplied by carboxylate groups during thermal decomposition of $\text{Fe}(\text{OL})_3$. Our interpretation of the pathway is also supported by the observation that the POV precursor suppresses formation of the wüstite Fe_{1-x}O phase, unlike in control experiments where $\text{Fe}(\text{OL})_3$ was thermally decomposed in the absence of the POV (Figure S13). This suggests that, when the POV precursor is included, the reaction with $\text{Fe}(\text{OL})_3$ generates Fe–V–O monomers, which promote nucleation of the V-doped spinel magnetite phase. The reaction of cyclic POVs with diverse metal cations in organic solvents has been documented, often resulting in macrocyclic, heterometallic structures that may be intriguing precursors for metal oxide NC synthesis.^{77–79}

CONCLUSIONS

Multi-metal oxide nanostructures that contain the element vanadium hold promise for developing technologies. The colloidal synthetic routes used for most other metal oxide systems, which permit morphology control, surface engineering, post-synthetic transformation, and solution processing, remain limited for those containing vanadium due to a lack of suitable molecular precursors for vanadium incorporation. Being generally intrigued by the structural likeness of polyoxometalates to polyhedral units within target metal oxides, we have established proof-of-principle here that POVs are viable precursors for delivering vanadium to metal oxide nanocrystals. First, we discovered that the tetraalkylammonium halide reagent AQ336 extracts aqueous VO_3^- ions into organic solvents, conferring the requisite solubility to POVs for nanocrystal synthesis. The reaction of our $\text{AQ336}^+\text{VO}_3^-$ precursor with $\text{Fe}(\text{OL})_3$ produced a mixture of ternary crystal phases, triclinic FeVO_4 , and spinel-type $\text{Fe}_{3-x}\text{V}_x\text{O}_4$ (where $x \approx 0.2$). FeVO_4 is a multiferroic semiconductor being considered for diverse green technologies, including photoelectrochemical water splitting, and is thus a high-profile synthetic target that will be the subject of ongoing studies.^{44–46} The valuable magnetic properties of nanocrystalline spinel ferrites and vanadates also warrant their synthetic development, and we found that vanadium incorporation into the lattice of Fe_3O_4 led to an increase in both the mass-normalized magnetization and blocking temperature relative to undoped magnetite. Doping was also found to increase the optical band gap in the visible region, making

these NCs potentially of value as semiconductor devices and photocatalysts.

Previously, binary mixtures of metal carboxylates^{80,81} and multi-metal oxygen clusters⁶⁸ have been used as precursors to ternary metal oxide NCs. Likewise, employing POVs enables routes to these oxide phases that are challenging to access as well-formed colloidal NCs. The emergence of POVs as precursors to multi-metal oxide NCs is a significant expansion of current synthetic capabilities and may be extensible to other systems, enabling for diverse applications. Additionally, the use of a phase transfer agent to bring water-soluble POVs into organic solvent may permit the potential of other polyoxometalates and NC precursors to be investigated. For instance, polyoxomolybdates and polyoxotungstates have polyhedral structures and reactivities that are similar to POVs^{40,41,49,82} and therefore similar potential as nanocrystal precursors. The many combinations of viable polyoxometalates with these known nanocrystal precursors have implications for targeting quaternary or higher-order compositions that are both tantalizingly complex and not yet possible.

ASSOCIATED CONTENT

Supporting Information

The Supporting Information is available free of charge at <https://pubs.acs.org/doi/10.1021/acs.chemmater.1c03371>.

Synthetic details of iron vanadium oxide colloidal nanocrystals and further characterization, including additional TEM images, photographs, X-ray diffraction, Raman spectra, HAADF-STEM-EDXS analysis, UV–vis spectra, magnetometry results, and X-ray fluorescence spectra (PDF)

AUTHOR INFORMATION

Corresponding Author

Matthew R. Buck – Chemistry Department, United States Naval Academy, Annapolis, Maryland 21402, United States; orcid.org/0000-0002-4132-9502; Email: mbuck@usna.edu

Authors

Adam J. Bicchì – Nanoscale Device Characterization Division, National Institute of Standards and Technology (NIST), Gaithersburg, Maryland 20899, United States; orcid.org/0000-0001-5663-2048
Lucas M. Johnson – Chemistry Department, United States Naval Academy, Annapolis, Maryland 21402, United States
Ashley B. Sweet – Chemistry Department, United States Naval Academy, Annapolis, Maryland 21402, United States
Luke J. Barrante – Chemistry Department, United States Naval Academy, Annapolis, Maryland 21402, United States
Eric M. Cal – Chemistry Department, United States Naval Academy, Annapolis, Maryland 21402, United States
Angela R. Hight Walker – Nanoscale Device Characterization Division, National Institute of Standards and Technology (NIST), Gaithersburg, Maryland 20899, United States; orcid.org/0000-0003-1385-0672

Complete contact information is available at:

<https://pubs.acs.org/doi/10.1021/acs.chemmater.1c03371>

Notes

Certain commercial equipment or materials are identified in this paper to adequately specify the experimental procedures.

In no case does the identification imply recommendation or endorsement by NIST nor does it imply that the materials or equipment identified are necessarily the best available for the purpose.

The authors declare no competing financial interest.

ACKNOWLEDGMENTS

A.J.B. and A.R.H.W. acknowledge the NIST Innovations in Measurement Science (IMS) program for funding. We thank Curt Richter, Steve Hudson, Jeff Fagan, June Lau, and John Bonevich for their assistance with instrumentation. M.R.B. gratefully acknowledges the Office of Naval Research (ONR) for support through several Junior Naval Academy Research Council Grants (Jr. NARC, 2019-2021) and the Defense Threat Reduction Agency (DTRA) for funding through the Service Academy Research Initiative (DTRA SARI). M.R.B. also sincerely thanks the Volgeneau Gift Fund for supporting this project.

REFERENCES

- (1) Park, Y.; McDonald, K. J.; Choi, K.-S. Progress in Bismuth Vanadate Photoanodes for Use in Solar Water Oxidation. *Chem. Soc. Rev.* **2013**, *42*, 2321–2337.
- (2) Sharp, I. D.; Cooper, J. K.; Toma, F. M.; Buonsanti, R. Bismuth Vanadate as a Platform for Accelerating Discovery and Development of Complex Transition-Metal Oxide Photoanodes. *ACS Energy Lett.* **2017**, *2*, 139–150.
- (3) Yan, Q.; Yu, J.; Suram, S. K.; Zhou, L.; Shinde, A.; Newhouse, P. F.; Chen, W.; Li, G.; Persson, K. A.; Gregoire, J. M.; Neaton, J. B. Solar Fuels Photoanode Materials Discovery By Integrating High-Throughput Theory and Experiment. *Proc. Natl. Acad. Sci.* **2017**, *114*, 3040–3043.
- (4) Lee, D. K.; Lee, D.; Lumley, M. A.; Choi, K.-S. Progress on Ternary Oxide-Based Photoanodes for Use in Photoelectrochemical Cells for Solar Water Splitting. *Chem. Soc. Rev.* **2019**, *48*, 2126–2157.
- (5) Nii, Y.; Sagayama, H.; Arima, T.; Aoyagi, S.; Sakai, R.; Maki, S.; Nishibori, E.; Sawa, H.; Sugimoto, K.; Ohsumi, H.; Takata, M. Orbital Structures in Spinel Vanadates AV_2O_4 ($A = Fe, Mn$). *Phys. Rev. B* **2012**, *86*, No. 125142.
- (6) Kismarahardja, A.; Brooks, J. S.; Zhou, H. D.; Choi, E. S.; Matsubayashi, K.; Uwatoko, Y. Dielectric Properties of Single Crystal Spinels in the Series FeV_2O_4 , MnV_2O_4 , and CoV_2O_4 in High Magnetic Fields. *Phys. Rev. B* **2013**, *87*, No. 054432.
- (7) Adachi, K.; Suzuki, T.; Kato, K.; Osaka, K.; Takata, M.; Katsufuji, T. Magnetic-Field Switching of Crystal Structure in an Orbital-Spin-Coupled System: MnV_2O_4 . *Phys. Rev. Lett.* **2005**, *95*, No. 197202.
- (8) Sarkar, S.; Saha-Dasgupta, T. Orbital Ordering in FeV_2O_4 : Spinel With Two Orbital Active Sites. *Phys. Rev. B: Condens. Matter Mater. Phys.* **2011**, *84*, No. 235112.
- (9) Rogado, N.; Lawes, G.; Huse, D. A.; Ramirez, A. P.; Cava, R. J. The Kagomé-Staircase Lattice: Magnetic Ordering in $Ni_3V_2O_8$ and $Co_3V_2O_8$. *Solid State Commun.* **2002**, *124*, 229–233.
- (10) Cabrera, I.; Kenzelmann, M.; Lawes, G.; Chen, Y.; Chen, W. C.; Erwin, R.; Gentile, T. R.; Leão, J. B.; Lynn, J. W.; Rogado, N.; Cava, R. J.; Broholm, C. Coupled Magnetic and Ferroelectric Domains in Multiferroic $Ni_3V_2O_8$. *Phys. Rev. Lett.* **2009**, *103*, No. 087201.
- (11) Helton, J. S.; Butch, N. P.; Pajerowski, D. M.; Barilo, S. N.; Lynn, J. W. Three-Dimensional Magnetism and the Dzyaloshinskii-Moriya Interaction in $S = 3/2$ Kagome Staircase $Co_3V_2O_8$. *Sci. Adv.* **2020**, *6*, No. eaay9709.
- (12) Liardet, L.; Hu, X. Amorphous Cobalt Vanadium Oxide as a Highly Active Electrocatalyst for Oxygen Evolution. *ACS Catal.* **2018**, *8*, 644–650.
- (13) Chakrapani, K.; Bendt, G.; Hajiyani, H.; Lunkenbein, T.; Greiner, M. T.; Masliuk, L.; Salamon, S.; Landers, J.; Schlögl, R.; Wende, H.; Pentcheva, R.; Schulz, S.; Behrens, M. The Role of Composition of Uniform and Highly Dispersed Cobalt Vanadium Iron Spinel Nanocrystals for Oxygen Electrocatalysis. *ACS Catal.* **2018**, *8*, 1259–1267.
- (14) Kim, T. W.; Choi, K.-S. Nanoporous $BiVO_4$ Photoanodes with Dual-Layer Oxygen Evolution Catalysts for Solar Water Splitting. *Science* **2014**, *343*, 990–994.
- (15) Gadiyar, C.; Strach, M.; Schouwink, P.; Loiudice, A.; Buonsanti, R. Chemical Transformations at the Nanoscale: Nanocrystal-Seeded Synthesis of β - $Cu_2V_2O_7$ with Enhanced Photoconversion Efficiencies. *Chem. Sci.* **2018**, *9*, 5658–5665.
- (16) Wang, W.; Zhang, Y.; Wang, L.; Bi, Y. Facile Synthesis of Fe^{3+}/Fe^{2+} Self-Doped Nanoporous $FeVO_4$ Photoanodes for Efficient Solar Water Splitting. *J. Mater. Chem. A* **2017**, *5*, 2478–2482.
- (17) Song, F.; Bai, L.; Moysiadou, A.; Lee, S.; Hu, C.; Liardet, L.; Hu, X. Transition Metal Oxides as Electrocatalysts for the Oxygen Evolution Reaction in Alkaline Solutions: An Application-Inspired Renaissance. *J. Am. Chem. Soc.* **2018**, *140*, 7748–7759.
- (18) Wu, L.; Mendoza-Garcia, A.; Li, Q.; Sun, S. Organic Phase Syntheses of Magnetic Nanoparticles and Their Applications. *Chem. Rev.* **2016**, *116*, 10473–10512.
- (19) Kang, D.; Kim, T. W.; Kubota, S. R.; Cardiel, A. C.; Cha, H. G.; Choi, K.-S. Electrochemical Synthesis of Photoelectrodes and Catalysts for Use in Solar Water Splitting. *Chem. Rev.* **2015**, *115*, 12839–12887.
- (20) McDonald, K. J.; Choi, K.-S. A New Electrochemical Synthesis Route for a BiOI Electrode and Its Conversion to a Highly Efficient Porous $BiVO_4$ Photoanode for Solar Water Oxidation. *Energy Environ. Sci.* **2012**, *5*, 8553–8557.
- (21) Lumley, M. A.; Choi, K.-S. Investigation of Pristine and (Mo, W)-Doped $Cu_{11}V_6O_{26}$ for Use as Photoanodes for Solar Water Splitting. *Chem. Mater.* **2017**, *29*, 9472–9479.
- (22) Qiu, Y.; Liu, W.; Chen, W.; Chen, W.; Zhou, G.; Hsu, P.-C.; Zhang, R.; Liang, Z.; Fan, S.; Zhang, Y.; Cui, Y. Efficient Solar-Driven Water Splitting by Nanocone $BiVO_4$ -Perovskite Tandem Cells. *Sci. Adv.* **2016**, *2*, No. e1501764.
- (23) Khan, I.; Qurashi, A. Shape Controlled Synthesis of Copper Vanadate Platelet Nanostructures, Their Optical Band Edges, and Solar-Driven Water Splitting Properties. *Sci. Rep.* **2017**, *7*, 14370.
- (24) Kuang, Y.; Jia, Q.; Ma, G.; Hisatomi, T.; Minegishi, T.; Nishiyama, H.; Nakabayashi, M.; Shibata, N.; Yamada, T.; Kudo, A.; Domen, K. Ultrastable Low-Bias Water Splitting Photoanodes Via Photocorrosion Inhibition and In Situ Catalyst Regeneration. *Nat. Energy* **2017**, *2*, 16191.
- (25) Seabold, J. A.; Neale, N. R. All First Row Transition Metal Oxide Photoanode for Water Splitting Based on $Cu_3V_2O_8$. *Chem. Mater.* **2015**, *27*, 1005–1013.
- (26) Boles, M. A.; Engel, M.; Talapin, D. V. Self-Assembly of Colloidal Nanocrystals: From Intricate Structures to Functional Materials. *Chem. Rev.* **2016**, *116*, 11220–11289.
- (27) Choi, J.-H.; Wang, H.; Oh, S. J.; Paik, T.; Sung, P.; Sung, J.; Ye, X.; Zhao, T.; Diroll, B. T.; Murray, C. B.; Kagan, C. R. Exploiting the Colloidal Nanocrystal Library to Construct Electronic Devices. *Science* **2016**, *352*, 205–208.
- (28) Boles, M. A.; Ling, D.; Hyeon, T.; Talapin, D. V. The Surface Science of Nanocrystals. *Nat. Mater.* **2016**, *15*, 141–153.
- (29) Steimle, B. C.; Fenton, J. L.; Schaak, R. E. Rational Construction of a Scalable Heterostructured Nanorod Mega-Library. *Science* **2020**, *367*, 418–424.
- (30) Cheon, J.; Manna, L.; Schaak, R. E. Why Do We Care About Studying Transformations in Inorganic Nanocrystals? *Acc. Chem. Res.* **2021**, *54*, 1543–1544.
- (31) Tappan, B. A.; Horton, M. K.; Brutchey, R. L. Ligand-Mediated Phase Control in Colloidal $AgInSe_2$ Nanocrystals. *Chem. Mater.* **2020**, *32*, 2935–2945.
- (32) Buck, M. R.; Bicchieri, A. J.; Schaak, R. E. Insights into the Thermal Decomposition of $Co(II)$ Oleate for the Shape-Controlled Synthesis of Wurtzite-Type CoO Nanocrystals. *Chem. Mater.* **2014**, *26*, 1492–1499.

- (33) Seo, J.-W.; Jun, Y.-W.; Ko, S. J.; Cheon, J. In Situ One-Pot Synthesis of 1-Dimensional Transition Metal Oxide Nanocrystals. *J. Phys. Chem. B* **2005**, *109*, 5389–5391.
- (34) Li, X.; Schaak, R. E. ZnO-Templated Synthesis and Metal-Insulator Transition of VO₂ Nanostructures. *Chem. Mater.* **2019**, *31*, 2088.
- (35) Bergerud, A.; Buonsanti, R.; Jordan-Sweet, J. L.; Milliron, D. J. Synthesis and Phase Stability of Metastable Bixbyite V₂O₃ Colloidal Nanocrystals. *Chem. Mater.* **2013**, *25*, 3172–3179.
- (36) Mantella, V.; Ninova, S.; Saris, S.; Loiodice, A.; Aschauer, U.; Buonsanti, R. Synthesis and Size-Dependent Optical Properties of Intermediate Band Gap Cu₃VS₄ Nanocrystals. *Chem. Mater.* **2019**, *31*, 532–540.
- (37) Zhang, S.; Li, Y.; Wu, C.; Zheng, F.; Xie, Y. Novel Flowerlike Metastable Vanadium Dioxide (B) Micronanostructures: Facile Synthesis and Application in Aqueous Lithium Ion Batteries. *J. Phys. Chem. C* **2009**, *113*, 15058–15067.
- (38) Zhang, S.; Shang, B.; Yang, J.; Yan, W.; Wei, S.; Xie, Y. From VO₂ (B) to VO₂ (A) Nanobelts: First Hydrothermal Transformation, Spectroscopic Study and First Principles Calculation. *Phys. Chem. Chem. Phys.* **2011**, *13*, 15873–15881.
- (39) Zhang, L.; Xia, F.; Song, Z.; Webster, N. A. S.; Luo, H.; Gao, Y. Synthesis and Formation Mechanism of VO₂(A) Nanoplates with Intrinsic Peroxidase-like Activity. *RSC Adv.* **2015**, *5*, 61371–61379.
- (40) Pope, M. T.; Müller, A. Polyoxometalate Chemistry: An Old Field with New Dimensions. *Angew. Chem., Int. Ed.* **1991**, *30*, 34–48.
- (41) Long, D.-L.; Burkholder, E.; Cronin, L. Polyoxometalate Clusters, Nanostructures and Materials: From Self-assembly to Designer Materials and Devices. *Chem. Soc. Rev.* **2007**, *36*, 105–121.
- (42) Petel, B. E.; Matson, E. M. Oxygen-atom Vacancy Formation and Reactivity in Polyoxovanadate Clusters. *Chem. Commun.* **2020**, *56*, 13477–13490.
- (43) Nguyen, T.-D.; Dinh, C.-T.; Do, T.-O. Monodisperse Samarium and Cerium Orthovanadate Nanocrystals and Metal Oxidation States on the Nanocrystal Surface. *Langmuir* **2009**, *25*, 11142–11148.
- (44) Gonzalez-Platas, J.; Lopez-Moreno, S.; Bandiello, E.; Bettinelli, M.; Errandonea, D. Precise Characterization of the Rich Structural Landscape Induced by Pressure in Multifunctional FeVO₄. *Inorg. Chem.* **2020**, *59*, 6623–6630.
- (45) Zhang, M.; Ma, Y.; Friedrich, D.; van de Krol, R.; Wong, L. H.; Abdi, F. F. Elucidation of the Opto-electronic and Photoelectrochemical Properties of FeVO₄ Photoanodes for Solar Water Oxidation. *J. Mater. Chem. A* **2018**, *6*, 548–555.
- (46) Bera, G.; Surampalli, A.; Mishra, A.; Mal, P.; Reddy, V. R.; Banerjee, A.; Sagdeo, A.; Das, P.; Turpu, G. R. Magnetolattice Coupling, Magnetic Frustration, and Magnetoelectric Effect in the Cr-Doped FeVO₄ Multiferroic Material and Their Correlation with Structural Phase Transitions. *Phys. Rev. B: Condens. Matter Mater. Phys.* **2019**, *100*, No. 014436.
- (47) Park, J.; An, K.; Hwang, Y.; Park, J.-G.; Noh, H.-J.; Kim, J.-Y.; Park, J.-H.; Hwang, N.-M.; Hyeon, T. Ultra-large-scale syntheses of monodisperse nanocrystals. *Nat. Mater.* **2004**, *3*, 891–895.
- (48) Ghosh, S.; Manna, L. The Many “Facets” of Halide Ions in the Chemistry of Colloidal Inorganic Nanocrystals. *Chem. Rev.* **2018**, *118*, 7804–7864.
- (49) Gumerova, N. I.; Rempel, A. Polyoxometalates in Solution: Speciation Under Spotlight. *Chem. Soc. Rev.* **2020**, *49*, 7568–7601.
- (50) Livage, J. Vanadium Pentoxide Gels. *Chem. Mater.* **1991**, *3*, 578–593.
- (51) Hamilton, E. E.; Fanwick, P. E.; Wilker, J. J. The Elusive Vanadate (V₃O₉)³⁻: Isolation, Crystal Structure, and Nonaqueous Solution Behavior. *J. Am. Chem. Soc.* **2002**, *124*, 78–82.
- (52) Fuchs, J.; Mahjour, S.; Pickardt, J. Structure of the “True” Metavanadate Ion. *Angew. Chem., Int. Ed.* **1976**, *15*, 374–375.
- (53) Testa-Anta, M.; Ramos-Docampo, M. A.; Comesana-Hermo, M.; Rivas-Murias, B.; Salguero, V. Raman Spectroscopy to Unravel the Magnetic Properties of Iron Oxide Nanocrystals for Bio-Related Applications. *Nanoscale Adv.* **2019**, *1*, 2086–2103.
- (54) Slavov, L.; Abrashev, M. V.; Merodiiska, T.; Gelev, C.; Vandenberghe, R. E.; Markova-Deneva, I.; Nedkov, I. Raman Spectroscopy Investigation of Magnetite Nanoparticles in Ferrofluids. *J. Magn. Magn. Mater.* **2010**, *322*, 1904–1911.
- (55) Zhang, A. M.; Liu, K.; Ji, J. T.; He, C. Z.; Tian, Y.; Jin, F.; Zhang, Q. M. Raman Phonons in Multiferroic FeVO₄ Crystals. *Chin. Phys. B* **2015**, *24*, 126301.
- (56) Kesavan, G.; Pichumani, M.; Chen, S.-M. Influence of Crystalline, Structural, and Electrochemical Properties of Iron Vanadate Nanostructures on Flutamide Detection. *ACS Appl. Nano Mater.* **2021**, *4*, 5883–5894.
- (57) Otero-Lorenzo, R.; Ramos-Docampo, M. A.; Rodríguez-Gonzalez, B.; Comesana-Hermo, M.; Salguero, V. Solvothermal Clustering of Magnetic Spinel Ferrite Nanocrystals: A Raman Perspective. *Chem. Mater.* **2017**, *29*, 8729–8736.
- (58) Zhao, Z.-W.; Wen, T.; Liang, K.; Jiang, Y.-F.; Zhou, X.; Shen, C.-C.; Xu, A.-W. Carbon-Coated Fe₃O₄/VO_x Hollow Microboxes Derived from Metal–Organic Frameworks as a High-Performance Anode Material for Lithium-Ion Batteries. *ACS Appl. Mater. Interfaces* **2017**, *9*, 3757–3765.
- (59) Beisinger, M. C.; Payne, B. P.; Grosvenor, A. P.; Lau, L. W.; Gerson, A. R.; Smart, R. S. C. Resolving Surface Chemical States in XPS Analysis of First Row Transition Metals, Oxides and Hydroxides: Sc, Ti, V, Cu and Zn. *Appl. Surf. Sci.* **2010**, *257*, 887–898.
- (60) Kumari, S.; Gutkowski, R.; Junquera, J. R. C.; Kostka, A.; Hengge, K.; Scheu, C.; Schuhmann, W.; Ludwig, A. Combinatorial Synthesis and High-Throughput Characterization of Fe–V–O Thin-Film Materials Libraries for Solar Water Splitting. *ACS Comb. Sci.* **2018**, *20*, 544–553.
- (61) Lamers, M.; Fiechter, S.; Friedrich, D.; Abdi, F. F.; van de Krol, R. Formation and Suppression of Defects During Heat Treatment of BiVO₄ Photoanodes for Solar Water Splitting. *J. Mater. Chem. A* **2018**, *6*, 18694–18700.
- (62) Tran-Phu, T.; Fusco, Z.; Di Bernardo, I.; Lipton-Duffin, J.; Toe, C. Y.; Daiyan, R.; Gengenbach, T.; Lin, C.-H.; Bo, R.; Nguyen, H. T.; Barca, G. M. J.; Wu, T.; Chen, H.; Amal, R.; Tricoli, A. Understanding the Role of Vanadium Vacancies in BiVO₄ for Efficient Photoelectrochemical Water Oxidation. *Chem. Mater.* **2021**, *33*, 3553–3565.
- (63) Bronstein, L. M.; Huang, X.; Retrum, J.; Schmucker, A.; Pink, M.; Stein, B. D.; Dragnea, B. Influence of Iron Oleate Complex Structure on Iron Oxide Nanoparticle Formation. *Chem. Mater.* **2007**, *19*, 3624–3632.
- (64) Bodnarchuk, M. I.; Kovalenko, M. V.; Groiss, H.; Resel, R.; Reissner, M.; Hesser, G.; Lechner, R. T.; Steiner, W.; Schaffler, F.; Heiss, W. Exchange-Coupled Bimagnetic Wustite/Metal Ferrite Core/Shell Nanocrystals: Size, Shape, and Compositional Control. *Small* **2009**, *5*, 2247–2252.
- (65) Pinchon, B. P.; Gerber, O.; Lefevre, C.; Florea, I.; Fleutot, S.; Baaziz, W.; Pauly, M.; Ohlmann, M.; Ulhaq, C.; Ersen, O.; Pierron-Bohnes, V.; Panissod, P.; Drillon, M.; Begin-Colin, S. Microstructural and Magnetic Investigations of Wustite-Spinel Core-Shell Cubic-Shaped Nanoparticles. *Chem. Mater.* **2011**, *23*, 2886–2900.
- (66) Smirnov, M. B.; Roginskii, E. M.; Smirnov, K. S.; Baddour-Hadjean, R.; Pereira-Ramos, J.-P. Unraveling the Structure–Raman Spectra Relationships in V₂O₅ Polymorphs via a Comprehensive Experimental and DFT Study. *Inorg. Chem.* **2018**, *57*, 9190–9204.
- (67) Tang, J.; Myers, M.; Bosnick, K. A.; Brus, L. E. Magnetite Fe₃O₄ Nanocrystals: Spectroscopic Observation of Aqueous Oxidation Kinetics. *J. Phys. Chem. B* **2003**, *107*, 7501–7506.
- (68) Sanchez-Lievanos, K. R.; Tariq, M.; Brennessel, W. W.; Knowles, K. E. Heterometallic Trinuclear Oxo-Centered Clusters as Single-Source Precursors for Synthesis of Stoichiometric Monodisperse Transition Metal Ferrite Nanocrystals. *Dalton Trans.* **2020**, *49*, 16348–16358.
- (69) Feng, J.; Wang, Z.; Zhao, X.; Yang, G.; Zhang, B.; Chen, Z.; Huang, Y. Probing the Performance Limitations in Thin-Film FeVO₄ Photoanodes for Solar Water Splitting. *J. Phys. Chem. C* **2018**, *122*, 9773–9782.

(70) Wei, D.; Huang, L.; Liang, H.; Zou, J.; Chen, W.; Yang, C.; Hou, Y.; Zheng, D.; Zhang, J. Photocatalytic Hydroxylation of Benzene to Phenol Over Organosilane-Functionalized FeVO₄ Nanorods. *Catal. Sci. Technol.* **2021**, *11*, 5931–5937.

(71) Taufiq, A.; Yuliantika, D.; Hariyanto, Y. A.; Hidayat, A.; Bahtiar, S.; Mufti, N.; Hidayat, N. Effect of Template on Structural and Band Gap Behaviors of Magnetite Nanoparticles. *J. Phys. Conf. Ser.* **2018**, *1093*, No. 012020.

(72) Saragi, T.; Depi, B. L.; Butarbutar, S.; Permana, B.; Risdiana. The Impact of Synthesis Temperature on Magnetite Nanoparticles Size Synthesized by Co-Precipitation Method. *J. Phys. Conf. Ser.* **2018**, *1013*, No. 012190.

(73) Sakthi Sri, S. P.; Taj, J.; George, M. Facile Synthesis of Magnetite Nanocubes Using Deep Eutectic Solvent: An Insight to Anticancer and Photo-Fenton Efficacy. *Surf. Interfaces* **2020**, *20*, No. 100609.

(74) He, Z.; Yamaura, J.-I.; Ueda, Y. Flux Growth and Magnetic Properties of FeVO₄ Single Crystals. *J. Solid State Chem.* **2008**, *181*, 2346–2349.

(75) Júnior, I. L.; Millet, J.-M. M.; Aouine, M.; do Carmo Rangel, M. The Role of Vanadium on the Properties of Iron Based Catalysts for the Water Gas Shift Reaction. *Appl. Catal. A: Gen.* **2005**, *283*, 91–98.

(76) Kwon, S. G.; Piao, Y.; Park, J.; Angappane, S.; Jo, Y.; Hwang, N.-M.; Park, J.-G.; Hyeon, T. Kinetics of Monodisperse Iron Oxide Nanocrystal Formation by “Heating-Up” Process. *J. Am. Chem. Soc.* **2007**, *129*, 12571–12584.

(77) Kurata, T.; Uehara, A.; Hayashi, Y.; Isobe, K. Cyclic Polyvanadates Incorporating Template Transition Metal Cationic Species: Synthesis and Structures of Hexavanadate [PdV₆O₁₈]⁴⁻, Octavanadate [Cu₂V₈O₂₄]⁴⁻, and Decavanadate [Ni₄V₁₀O₃₀(OH)₂(H₂O)₆]⁴⁻. *Inorg. Chem.* **2005**, *44*, 2524–2530.

(78) Inami, S.; Nishio, M.; Hayashi, Y.; Isobe, K.; Kameda, H.; Shimoda, T. Dinuclear Manganese and Cobalt Complexes with Cyclic Polyoxovanadate Ligands: Synthesis and Characterization of [Mn₂V₁₀O₃₀]⁶⁻ and [Co₂(H₂O)₂V₁₀O₃₀]⁶⁻. *Eur. J. Inorg. Chem.* **2009**, *34*, 5253–5258.

(79) Nishio, M.; Inami, S.; Katayama, M.; Ozutsumi, K.; Hayashi, Y. Lanthanide Complexes of Macrocyclic Polyoxovanadates by VO₄ Units: Synthesis, Characterization, and Structure Elucidation by X-ray Crystallography and EXAFS Spectroscopy. *Inorg. Chem.* **2012**, *51*, 784–793.

(80) Bao, N.; Shen, L.; Wang, Y.; Padhan, P.; Gupta, A. A Facile Thermolysis Route to Monodisperse Ferrite Nanocrystals. *J. Am. Chem. Soc.* **2007**, *129*, 12374–12375.

(81) Bao, N.; Shen, L.; An, W.; Padhan, P.; Heath Turner, C.; Gupta, A. Formation Mechanism and Shape Control of Monodisperse Magnetic CoFe₂O₄ Nanocrystals. *Chem. Mater.* **2009**, *21*, 3458–3468.

(82) Gumerova, N. I.; Rompel, A. Synthesis, Structures and Applications of Electron-Rich Polyoxometalates. *Nat. Rev. Chem.* **2018**, *2*, 0112.